ADVANCED FUNCTIONAL MATERIALS
www.afm-journal.de

Bioresorbable and Wireless Rechargeable Implanted Na-ion Battery for Temporary Medical Devices

*Vedi Kuyil Azhagan Muniraj, Bincy Lathakumary Vijayan, Hussien Hammoud, Roger Delattre, Marc Ramuz, Eve Djenizian, Eleonora Vandini, Daniela Giuliani, and Thierry Djenizian**

In this work, an alternative fabrication process is implemented to fabricate a bioresorbable Na-ion battery showing excellent electrochemical performance (discharge capacity of 5.1 mAh cm^{-2}) and no toxicity after being disintegrated under in vivo conditions. Solely composed of biocompatible materials, the proposed all-solid-state rechargeable battery implanted under the skin is capable of disintegrating safely. The operating days and lifetime of this novel energy storage system are evidenced that after being implanted in artificial skin can be finely controlled by tuning the thickness of the encapsulation layer, rendering possible the design of "on-demand" bio-eliminable batteries that may operate days or several weeks. The toxicity tests and the lack of organ damage performed by ex vivo analyses after 3 months confirmed the safety of the approach. In addition, wireless recharge of the battery is demonstrated through the skin using an inductive charger to establish the proof-of-concept. Preliminary tests revealed that wireless recharge of the subcutaneous implanted battery is achieved in 30 min, and that recharge remains possible in 1 h for deeper implanted batteries. The high versatility of the concept is definitely appealing to address the various needs of the temporary medical device market.

1. Introduction

Healthcare has undergone outstanding progress due to the emergence of biomedical implants like pacemakers, cochlear implants, visual prostheses, etc. More specifically, temporary medical devices (TMDs), ensuring a therapeutic function during a limited period of time, are under development to cure various injuries of the body as, for instance, electrical stimulators for nerve regeneration,[1] stroke recovery,[2] or bone fracture healing.[3] The future generation of TMDs is strongly desired to become smarter by disintegrating safely after use in order to avoid a second surgery for removal. Thus, bioresorbable electronics including electrodes, sensors, and integrated circuits have attracted attention and several achievements have been successfully reported.[4–6] Indeed, bioresorbable materials provide a unique opportunity to engineer new electrical, optical, and sensing components into in-vivo sensing systems that eliminate any boundary between target molecules and sensing devices, granting direct access to biofluids and acting as an in situ sentinel once implanted in the body, without the need of secondary device-retrieval surgery that may cause tissue lesion or infection. Bioresorbable materials can have a high potential in personalized medicine, especially for those treatments that benefit from a continuous and localized monitoring of specific analytes for a limited time, for example, chemotherapeutic cancer treatment, post-surgery sepsis, acute trauma treatment, pharmacokinetics profiling, and disease biomarker detection.

Today, energy sources to power TMDs mainly rely on rechargeable Li-ion batteries due to their high energy and power densities, versatility, and lifespan.[7,8] Unfortunately, these batteries are composed of toxic elements that cannot be safely degraded and must be then removed by surgery.[9] In addition, the battery recharge is achieved by external large chargers implying non-convenient wires passing through the skin[10] or having to be permanently worn by the patients in the battery-free configuration as it has been reported for powering a bioresorbable pacemaker.[4] Thus, efforts have been focused on designing batteries able to be degraded or resorbed in biological media although the full

V. K. A. Muniraj, B. L. Vijayan, H. Hammoud, R. Delattre, M. Ramuz, E. Djenizian, T. Djenizian
Mines Saint-Etienne
Department of Flexible Electronics
Center of Microelectronics in Provence
Gardanne F-13541, France
E-mail: thierry.djenizian@emse.fr
E. Vandini, D. Giuliani
Department of Biomedical
Metabolic and Neural Sciences
University of Modena and Reggio Emilia
Via G. Campi 287, Modena 41125, Italy
T. Djenizian
Center of Physical-Chemical Methods of Research and Analysis
Al-Farabi Kazakh National University
Tole bi str., Almaty 96A, Kazakhstan

The ORCID identification number(s) for the author(s) of this article can be found under https://doi.org/10.1002/adfm.202417353

DOI: 10.1002/adfm.202417353

bio-elimination of TMDs including an efficient energy solution with the same feature has not been clearly reported yet.

Current bioresorbable energy storage devices are typically based on primary batteries, i.e., nonrechargeable systems, using different electrode materials (e.g., Mg, Mo, AZ31, MnO_2, etc.)[11,12] and liquid electrolytes, often biological fluids like blood,[13] saliva,[14] and urine,[15] leading to fluctuating electrochemical performance due to the constant degradation of the electrodes while the battery is functioning. This effect is particularly significant for Mg-based systems.[16] Although solid-state and gel-like electrolytes have been proposed, by-product formation hinders electrode properties, the batteries are cumbersome, and most of the time cannot be recharged, limiting their practical use. The recent sodium-ion technology offers a promising alternative as the main components can be biocompatible owing to the use of safe elements like Na, Mn, Ti, P, etc.[17,18] In 2016, Kim and co-workers tested a biocompatible Na-ion battery composed of sodium titanium phosphate (NTP) as anode, melanin-based materials mixed with Ag nanowires as cathodes, and aqueous Na_2SO_4 as an electrolyte. A high initial capacity value was achieved by one full cell (78 mAh g^{-1} at 0.05 A g^{-1}) albeit no electrochemical performance and stability during cycling has been studied.[19] As a proof-of-concept, Zhang et al. realized symmetric Na-ion microbatteries constructed with heteronanomat bifunctional electrodes based on $Na_2VTi(PO_4)_3$ and hydrogel carrying NaCl as electrolyte. These systems revealed excellent electrochemical properties in terms of discharge capacity (54 mAh g^{-1} at 1C) and stability.[17] However, these examples of biocompatible batteries are not bioresorbable. In 2021, Mei et al. fabricated a bioresorbable battery by designing biodegradable fiber conductors incorporated with polydopamine/polypyrrole composite material as the anode and MnO_2 as the cathode, biodegradable chitosan as the separator, and body fluid as the electrolyte. Besides the relatively low discharge capacity achieved (25.6 mAh g^{-1} at 0.5 A g^{-1}), this wire-shaped Na-ion battery revealed important drawbacks like the too fast degradation under in vivo conditions (only a few days) and the need to use external wires passing through the skin to be recharged, naturally limiting the practical application.[10] As a general remark about implantable battery studies, clinical tests showing no alteration of organs are often not sufficiently investigated to unambiguously demonstrate the nontoxicity effect.

Compared to their biocompatible and biodegradable counterparts, achieving the fabrication of a high performance bioresorbable rechargeable battery with a defined lifetime is definitely highly challenging for many reasons: i) all chemical components must be biocompatible and easily eliminated by the biological fluids in a reasonable time without inducing any sign of inflammation and alteration of organs, ii) the lifetime of the implanted batteries must be tuned according to the targeted application, iii) all-solid-state systems must be envisioned because the use of aqueous electrolyte is not compatible with electrodes that are supposed to be disintegrated by the body fluids, iv) the battery must be wirelessly recharged in order to avoid wires piercing the skin, v) an alternative fabrication process should be established as bioresorbable current collectors like Mg foils are strongly oxidized when the deposition of electrode slurries is performed by conventional techniques used by the battery manufacturers.

In this work, a high electrochemical performance bioresorbable Na-ion battery has been achieved by overcoming the main challenges described above. This complete all-solid-state cell was obtained using solely nontoxic materials, i.e., $NaTi_2(PO_4)_3$-C (NTP-C) and $Na_{0.44}MnO_2$ (NMO) as active anode and cathode materials, respectively for the main electrode components and sodium alginate mixed with Na_2SO_4 salt as the gel polymer electrolyte. An alternative fabrication process based on the evaporation of Mg thin film as a current collector on pellet electrodes has been implemented in order to face the various issues that are encountered by classical methods. Ex vivo tests confirmed the lack of toxicity as well as the preservation of organs. We show that the operating days and disintegration starting time of the implanted battery in artificial skin can also be finely controlled by tuning the thickness of a bioresorbable encapsulation layer, which is definitely valuable for determining the lifetime of batteries according to the application needs. In addition, the wireless recharge of the battery through explanted skin has been also performed with an inductive charger specifically designed for this application, opening the path toward the implantation of a bio-eliminable system depicted in **Figure 1**. All these achievements render possible the technological transfer of this novel device at the industrial scale to address the market of bio-eliminable energy supply for TMDs.

2. Result and Discussion

2.1. Fabrication and Characterizations of the All-Solid-State Bio-Eliminable Battery

The bio-eliminable Na-ion battery proposed in this work is only composed of biocompatible materials for which their safety has been verified through the examination of toxicologic files established by the Institut National de Recherche et de Sécurité (INRS). Regarding the use of non-hydrosoluble materials, compounds showing small particle sizes were selected to facilitate their safe elimination by the body. Thus, $Na_{0.44}MnO_2$ (NMO) with an average particle size of 1.1 µm was considered as the positive electrode material. NMO is regarded as one of the most promising Na-ion cathodes owing to its low cost, simple preparation, large capacity (121 mAh g^{-1}), and high stability.[20,21] In addition, the wide tunnels in the NMO orthorhombic structure are favorable for transporting the relatively large Na^+ and capable of tolerating the stress generated during charging/discharging.[22] Similarly, a sodium superionic conductor (NASICON) rhombohedral $NaTi_2(PO_4)_3$ (NTP, 133 mAh g^{-1}) with an average particle size of 1.8 µm was selected as negative electrode material thanks to delivering high performance toward NMO.[20] Due to the low electronic conductivity of NTP, carbon composite NTP-C obtained by the solid-state sintering method was selected for the anode.[23] The active materials were then formulated as electrode slurries by mixing active materials with sodium alginate (SA) and carbon black with a particle size of ≈60 nm. SA was selected as it is not toxic and shows good solubility in water, low cost, biodegradability, and biocompatibility.[24,25] Electrodes were pre-administrated with gel electrolyte before the cell assembly to improve the ionic conductivity and durability of the battery. Such electrolytes infused into electrodes form a catholyte (electrolyte added to cathode) and anolyte (electrolyte added to anode), respectively,

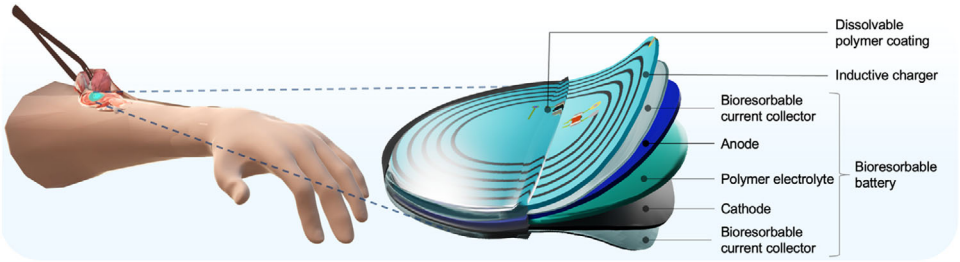

Figure 1. Schematic representation of an implantable all-solid-state bio-eliminable battery for TMDs. The concept relies on a bioresorbable Na-ion battery coupled to an inductive charger to ensure wireless recharge. A dissolvable polymer coating is used to control the lifetime of the implanted system.

creating a unified ion transport pathway.[26–29] This approach further improves the contact between the solid electrolyte and the active electrode materials, reducing interfacial resistance and increasing the overall efficiency and durability of the battery.[30–32]

Among the most known bioresorbable metals like W, Zn, Fe, and Mo that could be used as current collectors, Mg has been selected for several reasons:[33] i) Mg possesses the highest electrical conductivity, which improves the overall performance of the battery. ii) It also reveals the fastest dissolution rate of ≈0.05–0.5 µm h^{-1} in aqueous media allowing the design of a battery with a predefined lifetime thanks to the only control of the encapsulation layer thickness. iii) Mg is lighter than the other metals, which is particularly beneficial for implantable devices where weight reduction is important to avoid tissue stress or discomfort. iv) Mg has already been extensively studied and clinically tested in bioabsorbable applications such as orthopedic implants and vascular stents due to its biocompatibility and degradability properties. This existing knowledge base enables the conversion of magnesium into bioabsorbable battery systems, providing an easier path to regulatory approval compared to less studied materials. However, deposition of electrode slurries on Mg foil cannot be realized by classical approaches because this low potential metal is strongly subjected to oxidation reactions, affecting significantly the electrochemical properties of the battery. This is the reason why we investigated an alternative method based on the fabrication of pellet electrodes onto which an Mg thin film of 600 nm in thickness was evaporated. **Figure 2** depicts the main fabrication steps of the full all-solid-state battery that can be summarized as 1) fabrication of anode (≈430 µm thick) and cathode (≈780 µm thick) pellets by hydrodynamic press, 2) electrolyte-impregnated electrode by drop-casting, 3) Mg thin-film evaporation on electrodes after the cell-assembling using a ≈20 µm thick gel electrolyte acting also as separator. Besides saving metals and optimizing the electrochemical properties, it is important to note that H_2 bubbles appearing as side reactions during the dissolution of Mg are strongly minimized when the metal is in the form of a thin layer, which is definitely more suitable for degradable implants. This process was found sufficiently reliable to produce complete all-solid-state Na-ion cells as a disk of 0.74 cm in diameter, 1.2 mm in thickness, and weight ≈90 mg.

The morphological and chemical analysis of the all-solid-state Na-ion battery was performed by Scanning Electron Microscopy (SEM) and Energy-Dispersive X-ray Spectroscopy (EDX). The surface of the pellet electrodes before and after Mg thin-film deposition are shown in Figure S1 (Supporting Information). The rugosity of the electrode surfaces obtained by the hydraulic press is smooth enough to act as a suitable substrate for the subsequent uniform deposition of the 600 nm thick Mg layer as is confirmed by the examination of the cross-sectional SEM views of the Mg-coated NTP-C and NMO electrodes, respectively (See **Figure** 3a,b). Such a uniform Mg coating used as a current collector is supposed to ensure optimal electrical conductivity for stable battery operation. In order to have an insight into the electrode/electrolyte interfaces, the assembled battery was frozen, cut (snapped), and polished. The cross-sectional SEM view of the battery core shown in Figure 3c reveals an all-in-one integration of the ≈20 µm thick solid electrolyte with both the NTP-C and NMO electrode surfaces. This well-compacted interface property is crucial for ensuring efficient ionic transport and thus stable battery performance. The chemical mapping carried out by EDX analysis (Figure 3d–i) revealed the presence of key elements through the cross-section of the battery core. Specifically, the distribution of Mn from NMO, Na from the electrolyte, Ti from NTP-C, along with C, O, and P can be easily identified. An overlaying SEM image with elements identified, depicted in Figure 3j, facilitates the clear distinction of the battery components, highlighting the spatial distribution of these elements within the cross-section.

The performance of the Na-ion battery evaluated by electrochemical techniques is summarized in **Figure** 4. For more information, the capacities are expressed in gravimetric and volumetric units (see Figure S2a–f, Supporting Information). The first galvanostatic charge-discharge (GCD) curves recorded at C/5 rate (Figure 4a) revealed a high discharge capacity of 5.1 mAh cm^{-2}. The GCD profile of NMO versus NTP-C using a gel electrolyte displayed curves characterized by multiple redox reactions within a potential range of 0–1.5 V, similar to the behaviors reported for aqueous electrolytes.[18] From the derivative plot of the charge-discharge curve (dQ/dV), three main peaks labeled as 1, 2, and 3 (and their complementary noted 1′, 2′, and 3′) are easily identified (Figure 4b). These peaks correspond to different reversible phase transitions of NMO during the insertion and extraction of Na^+ ions occurring via the tunnel-type Na2 sites in the NMO structure (see Figure S2g, Supporting Information).[18,34,35] GCD curves were recorded at various C-rates to assess the rate capability, as shown in Figure 4c. These results show that the battery can be cycled at different rates up to 4C, i.e., charging and discharging in 15 min. The corresponding capacity values over 60 cycles were plotted in Figure 4d. The electrochemical performance shows that the battery is capable of maintaining substantial capacity even at fast kinetics, highlighting its robustness

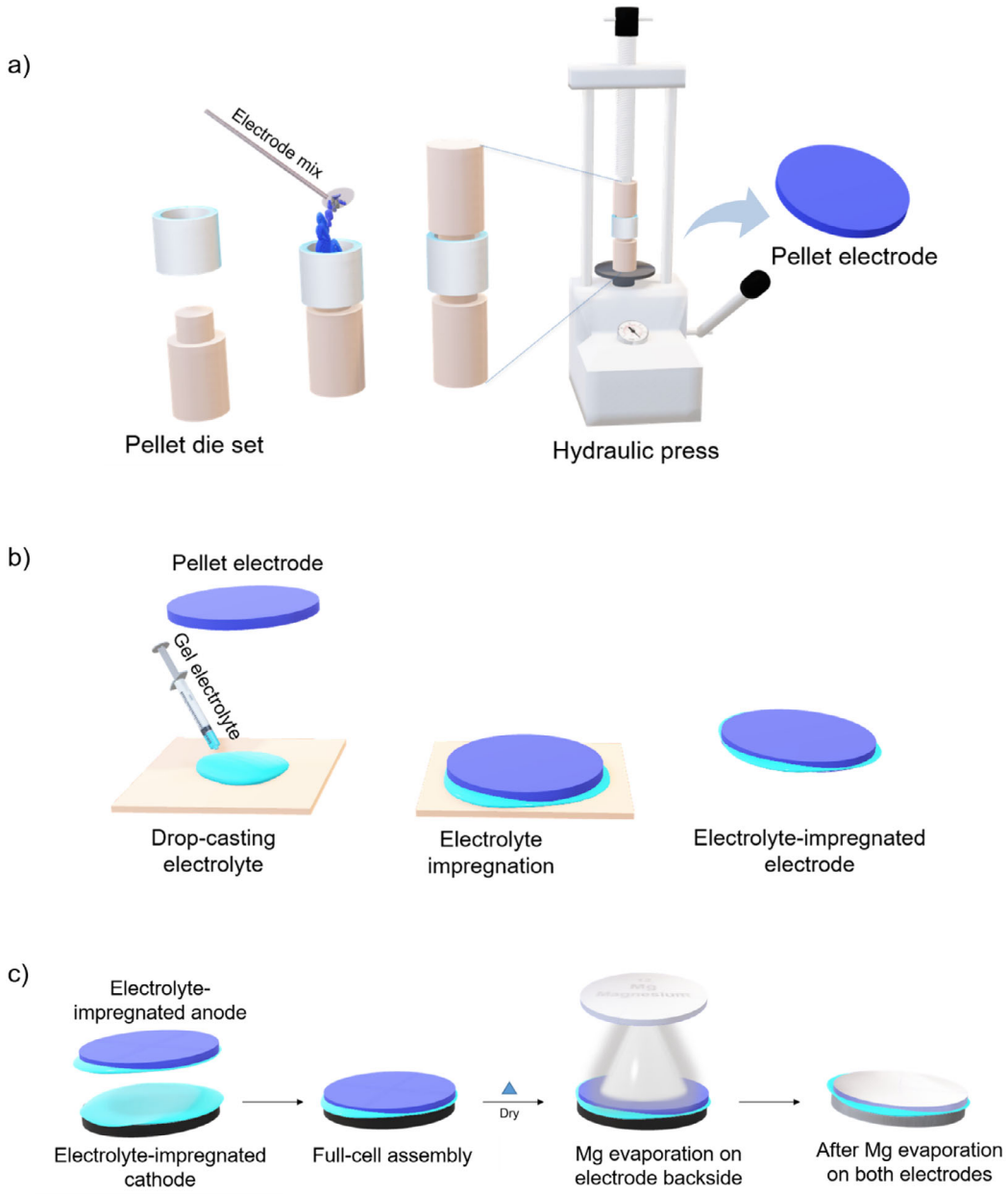

Figure 2. Schematic of the bioresorbable battery fabrication sequence. a) formation of pellet electrodes by hydraulic press machine, b) impregnating drop-casted gel electrolyte onto the electrode, c) assembly of the full cell and evaporation of Mg thin-film on both remaining electrode faces.

under varying operational conditions. Cycling stability was further evaluated at a 2C rate over 100 cycles. As shown in Figure 4e, the battery retained 83% of its initial capacity. The coulombic efficiency (CE) remained consistent at 98% throughout the 100 cycles, reinforcing the battery efficiency and reliability under cycling conditions. The capacity fading observed after 100 cycles can be attributed to the high reactivity of Mg that is subjected to oxidation processes. It can be noticed that the use of more stable bioresorbable current collectors like Mo could be envisioned to increase stability during cycling. But in the light of the targeted applications, the electrochemical performance achieved in this work is acceptable as the capacity fading is less than 20% of the initial capacity over 100 cycles rendering the battery operating for 3 months in the case of a daily recharge.

Electrochemical impedance spectroscopy (EIS) was performed to evaluate the internal resistance of the battery. The Nyquist plots of EIS results given in Figure 4f and Randle's equivalent circuit model were simulated to study the experimentally obtained impedance spectra. The simulated result revealed a semicircle at the high-frequency region with minimal series (R1) and charge transfer (R2) resistances of ≈11 and 32 Ω, respectively. These results highlight the superior electrochemical activity of the bioeliminable battery, characterized by a low internal resistance that

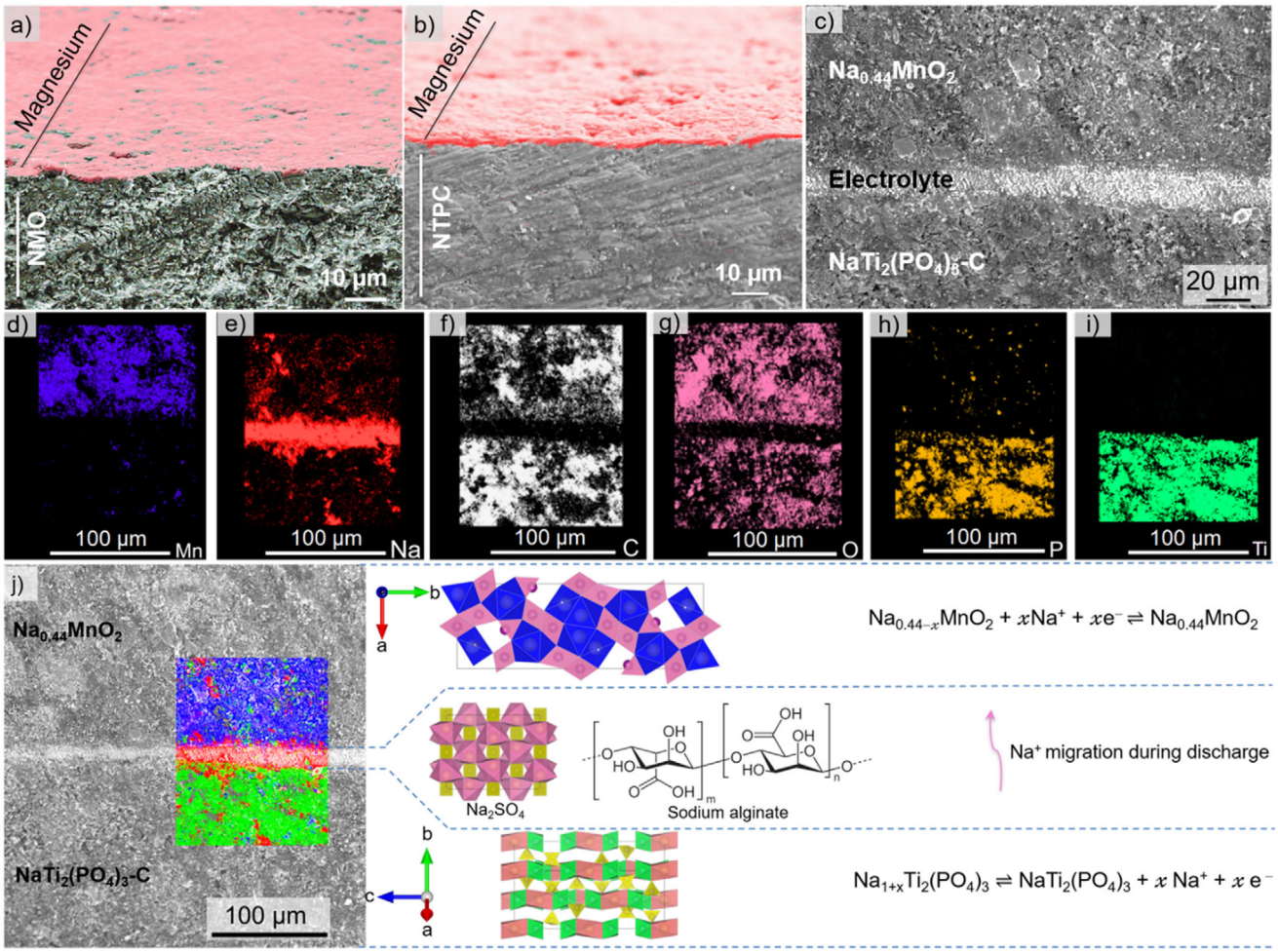

Figure 3. a) and b) SEM images of Mg thin-films (600 nm) evaporated on the NMO and NTP-C electrode surfaces, respectively. c) Cross-sectional SEM view of the all-solid-state full cell. d–i) Chemical mapping by EDX shows the presence of predominant elements in the different parts of the battery. j) Cross-sectional EDX map revealing distinct layers through color-coded elements overlaid on the SEM image, and the corresponding reaction mechanisms occurring at the electrodes during the discharge process.

can be attributed to the efficient interface established between the electrolyte and the electrodes.

A comparative study including our work has been provided in **Tables** 1 and 2 in order to have better insight into the electrochemical performance of the different batteries reported so far.

2.2. Biological Studies

2.2.1. Disintegration Study of As-Prepared Batteries in Biological Media

The battery features in different biological media were studied by in vitro and in vivo tests. First, the as-fabricated battery was immersed in a Phosphate Buffered Saline (PBS) solution at 37 °C to analyze the progress of disintegration under in vitro conditions (**Figure** 5a–e). It is clearly apparent that the degradation time is extremely fast; actually, the battery is damaged almost immediately (Figure 5b) and it is then completely decomposed after just 1 h (Figure 5e). Definitely, such a very fast disintegration behavior is an asset for practical applications. Indeed, the design of batteries with predefined functioning time before being eliminated can be envisioned as the starting of disintegration will be controlled by the thickness of the subsequent soluble encapsulation layer (see the next section). One can notice that a black powder resulting from the disintegrated battery sedimented at the bottom of the flask showing that the battery components are dissociated but not dissolved in a static PBS solution.

Regarding in vivo tests, as-prepared batteries were implanted in the back of mice as illustrated in Figure 5f to verify the rapid disintegration as well as the efficient resorption by the body without any sign of toxicity. During the pilot study, we observed the back skin of the implanted mice at three different time points (namely, 24 h, 3 months, and 1 year after implantation) to investigate the bio-disintegration and bio-elimination of the battery, and the animal survival. We could notice that after 24 h the battery was no longer present in its initial shape but is fully disintegrated (Figure 5g), as well as 3 months (Figure 5h), and 1 year (Figure 5i) after implantation. In addition, mice survival was guaranteed at all 3 time points. The only raised parameter was the presence of

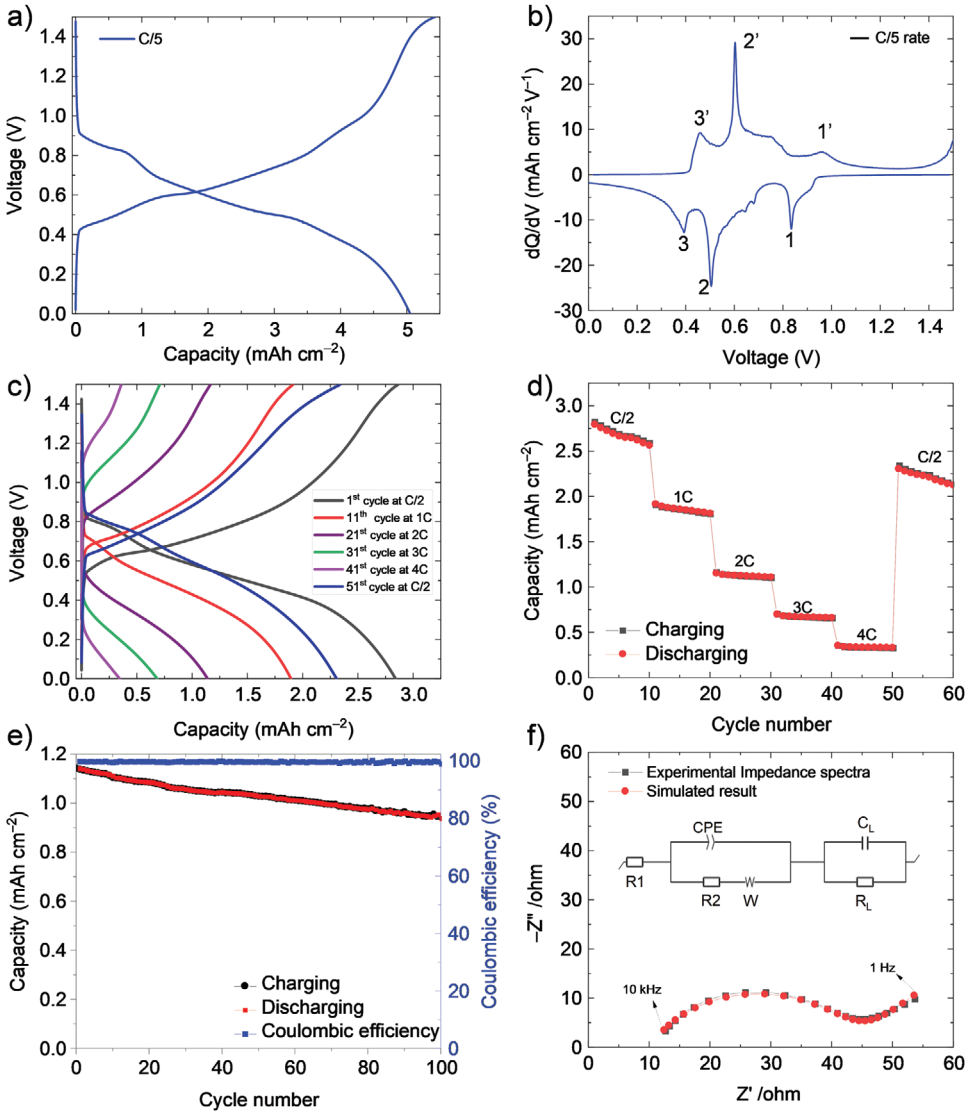

Figure 4. a) Galvanostatic charge-discharge (GCD) curves recorded for the bioresorbable battery at C/5 rate. b) dQ/dV derivative plot corresponding to the GCD profile recorded at C/5. c) GCD graphs recorded at various charge kinetics. d) Electrochemical performance at various kinetics for 60 cycles. e) Stability and coulombic efficiency of the battery at 2C rate for 100 cycles. f) Nyquist plot obtained by EIS within a frequency range of 10 kHz to 1 Hz and the corresponding equivalent circuit.

a black spot due to the remaining carbon black that coloring the skin. Indeed, post-mortem EDX elemental analyses performed on the skin that was exposed to the battery disintegration revealed no difference with the non-implanted counterpart, i.e., Mg, P, Ti, and Mn signals have not been detected, confirming that carbon is the only element that is not completely eliminated after 3 months (Figure 5j,k). The detailed study by EDX is given in Figure S3, Tables S1 and S2 (Supporting Information). However, the black spot became smaller and lighter after 1 year of monitoring, confirming that also carbon black is eliminated in the long term by the body fluids. It is important to mention that such an effect is not detrimental to the targeted application because carbon black is widely used as the pigment ink for tattoos.[43] Moreover, the black area is not visible when the suture is closed.

2.2.2. In Vivo Tests for Confirming the Nontoxicity of Implanted Battery

To assess the biocompatibility of the battery in vivo, during the whole experimental period, we monitored several parameters of general integrity that are the first to change in the event of any type of toxicity with the Shirpa test. Shirpa is a rapid battery of tests comprising 42 measurements of motor activity, coordination, postural control, muscle tone, autonomic functions, and emotional reactivity, as well as reflexes dependent on visual, auditory, and tactile modalities. Most of the measures in the battery are susceptible to change after gene modifications but also physiological alterations.[44] With these tests, we were able to distinguish physiological aspects or behaviors from those related to local or systemic toxicity. We analyzed macro-parameters such

Table 1. Description of few implantable batteries reported for powering TMDs.

Battery system	Electrode materials	Electrolyte	Encapsulation	Main features	Refs.
Primary battery	Mg and MoO_3	Sodium alginate with PBS	Polyanhydride and PLGA	Bioresorbable	[11]
	Mg and iodine/carbon black	Choline chloride/urea	Polyanhydride	Bioresorbable	[36]
	Mg and Fe	PBS	Polycaprolactone	Biodegradable	[37]
	AZ31, Au-SF	SF-[Ch][NO_3]	SF	Biodegradable	[38]
	Activated carbon and λ-MnO_2	Aqueous Na_2SO_4	Gelatin	Biodegradable	[39]
	Mg and Fe, Mo & W	PBS	PDMS	Biodegradable	[40]
	Zn and Nafion & Hb	PBS	NA	NA	[13]
	AZ31 vs SF -PPy	PBS	NA	Partially biodegradable	[41]
Secondary battery	Symmetric $Na_2VTi(PO_4)_3$	NaCl Hydrogel electrolyte	Silk fibroin hydrogel	Biocompatible Non bioresorbable	[17]
	NTP & synthetic melanin	Aqueous Na_2SO_4	NA	Biocompatible Non bioresorbable	[19]
	Polydopamine/polypyrrole and MnO_2	Chitosan separator with body fluid as electrolyte	Chitosan	Bioresorbable Non rechargeable under in-vivo conditions	[10]
	NTP-C & NMO	Na_2SO_4 and sodium alginate gel electrolyte	PLGA	Bioresorbable Wireless rechargeable	This work

as activity status, tremor, lacrimation, eyelid closure, fur appearance, whisker movement, and defecation. No alterations of the animal's status were found after 3 months from the implantation showing no toxicity due to the presence of the battery (data not shown).

Furthermore, the weight of the animals was checked throughout the entire experimental period and, besides physiological weight gain over time, no statistical difference between sham mice and mice implanted with the battery was found (**Figure 6**a).

To exclude an acute inflammatory reaction due to the implantation, body temperature was measured at different time points (namely, before implant, 24, 48, 72 h, 7 and 14 days after implant) and only 24 h after surgery, the temperature of mice implanted with battery is higher compared to that of a sham as a normal replay of the body to implantation (Figure 6b).

Systemic toxicity was also evaluated through the open field behavioral test (OF) observing changes in locomotion and anxiety. It was performed before surgery procedures as the baseline and at 30, 60, and 90 days after implantation. Total distance traveled and maximum speed (Figure 6c,d), as well as anxiety, measured as a percentage of time spent in the center (Figure 6e), were not affected at 3 months after implant, showing no toxicity due to the presence of the battery.

2.2.3. Ex Vivo Tests for Confirming the Non-Toxicity of Implanted Battery

During the sacrifice, organs (liver, spleen, kidney, heart, lung, brain, and back skin) were collected and weighed, and no significative macroalterations of their status have been found in both experimental groups (**Figure 7**a) to confirm the lack of toxicity of the implanted battery.

Impaired liver functions are a clear sign of systemic toxicity, for this reason, serum samples were analyzed to evaluate Alanine transaminase (ALT) levels for checking hepatic toxicity. No significant modification of ALT hepatic enzyme value was found in both groups of mice (Figure 7b) affirming that the implant of the battery did not create any systemic alteration.

Transversal kidney sections were cut at a cryostat into 20 µm slices and colored with haematoxylin and eosin staining. The number of glomeruli and their area were assessed for each section and no significant differences were found between implanted and sham mice (Figure 7c,d). In addition, there were no morphological alterations of the tissue, demonstrating that organ function is not impaired (Figure 7e).

Furthermore, to exclude local toxicity on the implant site, skin samples of the back of mice were analyzed. Transversal skin sections were cut at a cryostat into 40 µm slices and colored with haematoxylin and eosin staining. As shown in Figure 7f all battery-implanted animals displayed black deposits on the implant site due to the release of black carbon, but histological evaluation showed that skin thickness and layer distribution were not altered compared to sham mice, confirming that there were no local modifications of the tissue (Figure 7g,h). Furthermore, no residues of the battery were found, confirming its complete bioresorption after 3 months. To summarize, the results on the kidney (and skin) already evidence that there was no systemic and/or local toxicity.[5] We also evaluated hepatic markers, specifically Serum Alanine Transaminase (ALT) levels, whose increase is associated with hepatic toxicity, and we found no significant alterations, demonstrating no hepatotoxicity.[45] At this stage, according to the literature, all results we obtained so far (skin, kidney, and liver) are sufficient to confirm the lack of toxicity.

In terms of the biodegradable mechanism, the clearance of administered micro/nanoparticles from the circulation and their elimination from the body generally occurs via 2 main routes: renal excretion and hepatobiliary excretion. According to recent studies, smaller particles measuring a few tens of nanometers can be cleared through renal filtration, while larger particles are primarily excreted via the liver as feces. As stated by Adhipandito et al. in a review article, particles sized 6–8 nm are prone

Table 2. Electrochemical performance of different implantable batteries.

Anode vs cathode	Electrolyte	Working potential [V]	Capacity		Energy density			Power density			Refs.
			mAh g^{-1}	mAh cm^{-2}	Wh kg^{-1}	mWh cm^{-2}	mWh cm^{-3}	W kg^{-1}	mW cm^{-2}	mW cm^{-3}	
Primary battery system											
Mg vs MoO_3	SA/PBS	1.6	748.8	6.5	823.7	7.15	NA	NA	NA	NA	[11]
Mg vs iodine/CB	Choline chloride/urea	1.8	204	9.8	367	17.7	93.0	14.5	0.7	3.8	[36]
Mg vs Fe	PBS	0.7	1060	NA	694	NA	NA	NA	NA	NA	[37]
AZ31 vs Au-SF	SF-[Ch][NO_3]	1.4	NA	0.06	NA	0.078	70.9	NA	NA	1.07	[38]
AC vs λ-MnO_2	Na_2SO_4	0.6	9.58	407	NA	NA	NA	NA	NA	NA	[39]
Mg vs Mo	PBS	0.75	276	2.4	207	1.8	NA	NA	NA	NA	[40]
AZ31 vs SF -PPy	PBS	1.29	NA	4.42	NA	4.70	NA	NA	0.065	NA	[41]
Melanin vs λ-MnO_2	Na_2SO_4	1.03	16.1	NA	16.6	NA	NA	NA	NA	NA	[42]
Secondary battery system											
Symmetric $Na_2VTi(PO_4)_3$	NaCl hydrogel	1.5	54.1 @ 1C	NA	NA	NA	NA	NA	NA	NA	[17]
NTP & synthetic melanin	Na_2SO_4	0.5	78 @0.05 A g^{-1}	NA	NA	NA	NA	NA	NA	NA	[19]
Polydopamine/polypyrrole vs MnO_2	Body fluid	1.2	25.6 @0.5 A g^{-1}	NA	NA	NA	NA	NA	NA	NA	[10]
NTP-C vs NMO	SA /Na_2SO_4	1.5	78 @ C/5	5.1@ C/5	47	3.0	25.3	15.9	1.0	8.5	This work

to be easily cleared via urine and indicated the possibility for larger nanoparticles, even those in the 100–240 nm can be excreted through urine despite their relatively large size.[46] Additionally, Croissant et al. observed that nanoparticles larger than 10 nm or composed of heavy metals can be rapidly and efficiently uptaken by the liver and spleen.[47] Li et al. emphasized the central role of the liver in removing endogenous compounds from the blood, reporting that the hepatobiliary pathway was the primary route for eliminating gold nanoparticles.[48] In this process, nanoparticles enter the liver sinusoid, passively diffuse into hepatocytes via the Disse space, are transported into bile, and are ultimately eliminated via feces. Our in vivo experiments demonstrated that in the implant area, no materials are present after 12 weeks. Furthermore, the ex vivo analysis of the liver and histological analysis of skin and kidney showed that these organs remained unaltered, indicating the safety of materials and clearance of nano/microparticles through renal and/or hepatic processes. Based on these results and in regards to the literature data, one can assume that the water-soluble components of the battery (Mg, Na-alginate, Na_2SO_4, PBS, and PLGA) should be easily eliminated by urine/feces while the nonhydrosoluble micro/nanoparticles (NTPC, NMO, and carbon black) should enter the biological fluid circulation after electrode disintegration, before being subsequently eliminated mostly through hepatic processes.

2.3. Controlling the Disintegration Time of the Battery

As previously mentioned in part 2.2.1, the rapid disintegration time of the battery (only 1 h in vitro) is particularly interesting because the lifespan of the implanted battery can be simply controlled by tuning the thickness of a soluble encapsulation layer. Poly(lactic-co-glycolic) acid (PLGA) is widely used for medical applications due to its biocompatibility and degradability by hydrolysis in biological media. In this work, the dip-coating technique was used to encapsulate the batteries by PLGA layers showing different thicknesses. First, the in vitro disintegration of PLGA-coated batteries was investigated in PBS solution (static solution). From **Figure** 8a–d, the battery coated by a 40 µm thick PLGA layer is fully disintegrated after 14 days. In addition, 35 days is required to disintegrate a battery covered by a 110 µm thick PLGA thin film (Figure 8e–h). These results evidence that PLGA is able to delay significantly the degradation process and the thicker the PLGA layer, the longer the disintegration time. Thus, the control of the degradation time can be finely tuned rendering possible the fabrication of a battery with a determined lifetime once it is implanted.

Preliminary in vivo experiments also seem to confirm the results obtained in vitro. Indeed, disintegration time delay increases with the PLGA thickness (40, 110, 250 µm) for at least up to 3 weeks when the batteries are protected by PLGA coatings (data not shown, representative images in **Figure** 9). Compared to the bare battery that has been disintegrated in just 1 day, a 250 µm PLGA thick layer is able to preserve the device for several weeks. Therefore, controlling the thickness of the encapsulation layer opens the path to the design of "on-demand" bioresorbable batteries owing to a determined lifetime in the body after being implanted, which is definitely interesting in addressing the various needs of TMDs. Furthermore, we can notice that until the

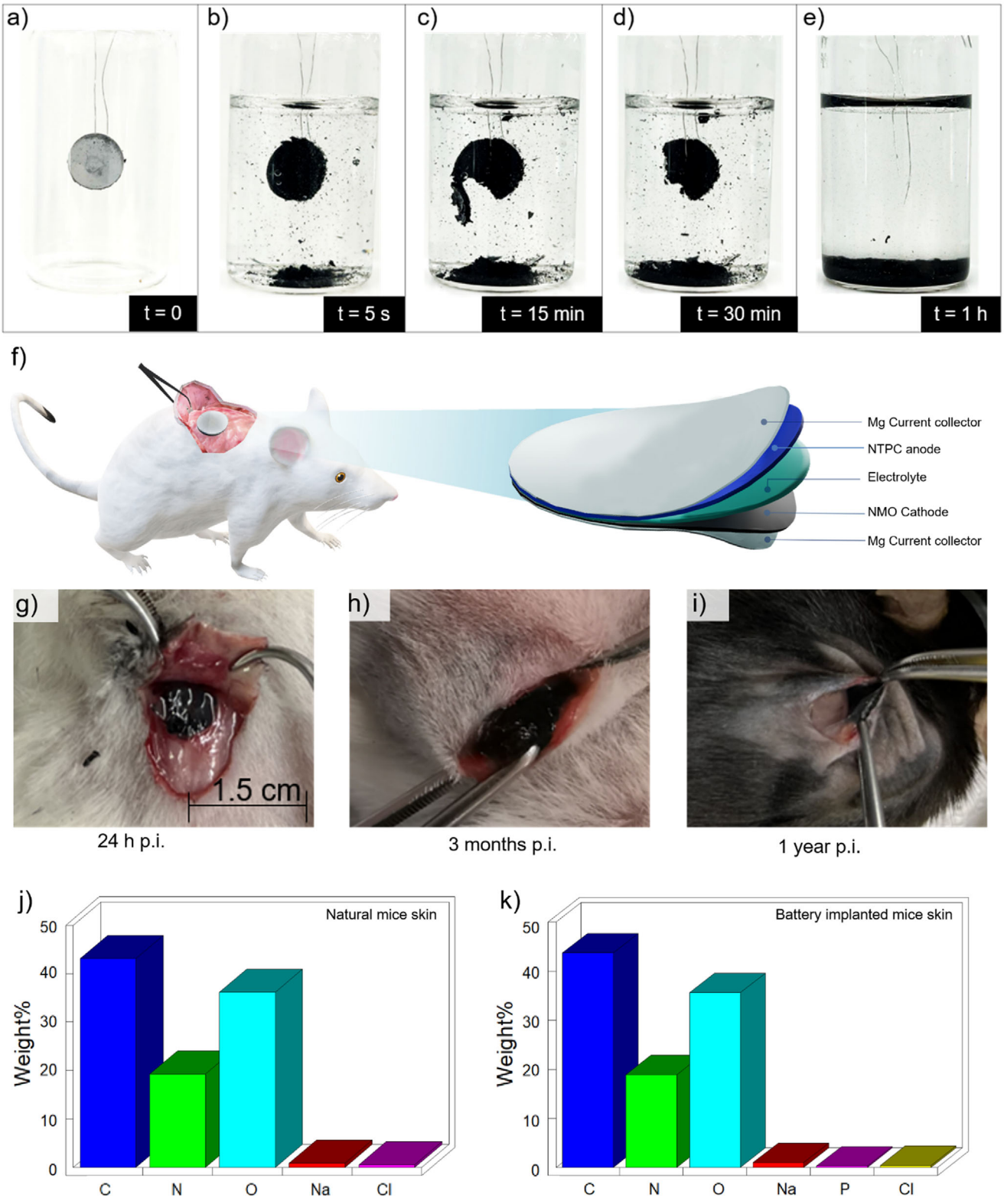

Figure 5. a–e) Disintegration evolution of the battery in a PBS solution at 37 °C. f) Schematic illustration of the subcutaneous implantation of the battery in a mouse. g-i) Representative images of back skin mice showing the disintegration evolution of the battery under in vivo conditions. The black spot due to the remaining carbon black is almost eliminated after one year. (Scale bar = 1,5 cm; p.i. = post-implant). EDX elemental analyses of the skin mice j) non-implanted and k) after the disintegration of the battery.

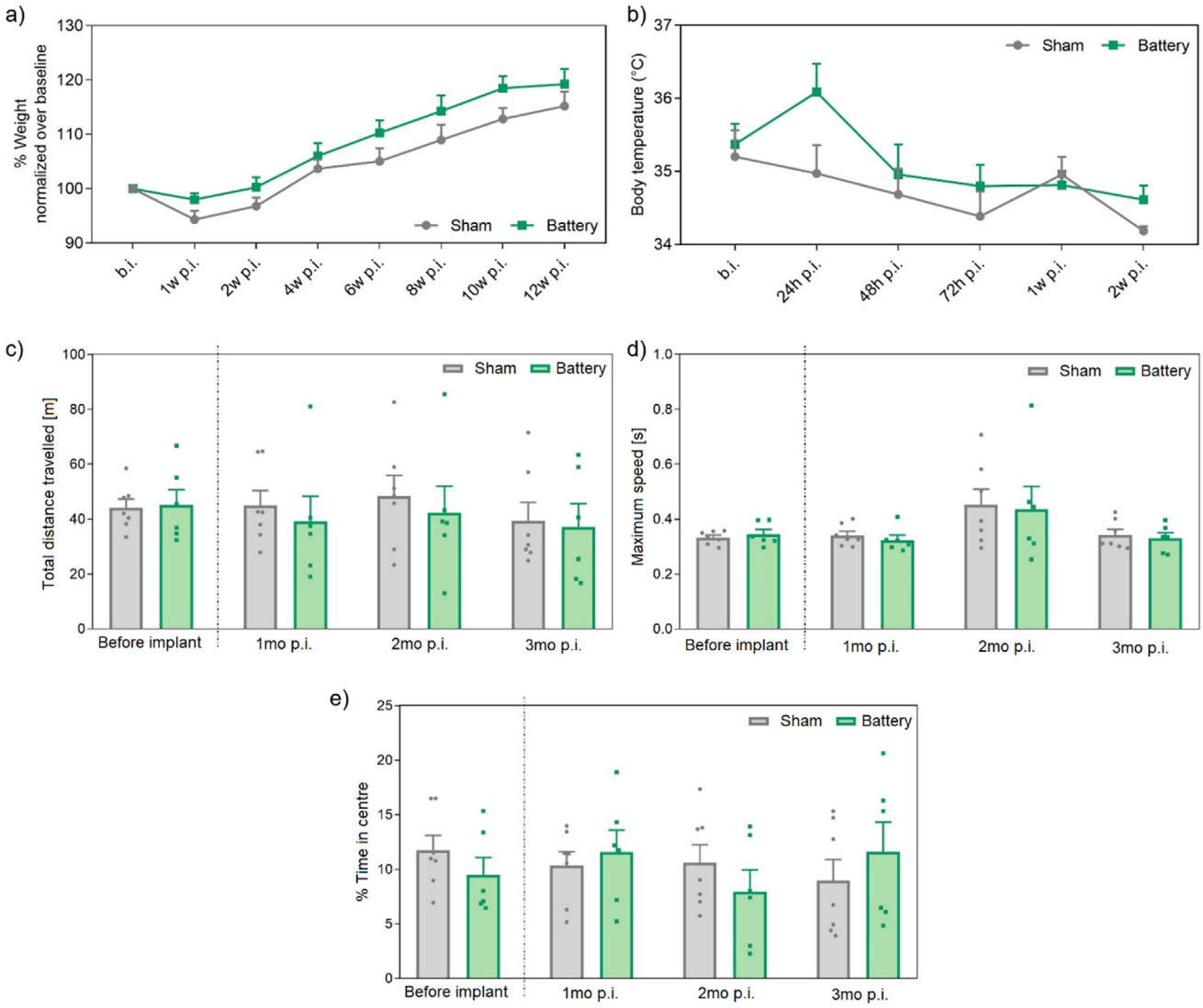

Figure 6. a) Weight variation over time (12 weeks) of all experimental groups. Data represented as mean ± standard error (SE) and analyzed with repeated measures two-way ANOVA considering $p < 0.05$ as significative (interaction $p = 0.7548$, time $p < 0.0001$, type of implant $p = 0.1555$). b) Body temperature variation over time (2 weeks) of all experimental groups. Data represented as mean ± SE and analyzed with repeated measures two-way ANOVA considering $p < 0.05$ as significative (interaction $p = 0.2435$, time $p = 0.0018$, type of implant $p = 0.1406$). c) Total distance traveled, d) Maximum speed, and e) % of the time in the center of OF test 1, 2, 3 months (mo) after implant. Data represented as mean ± SE and analyzed with nonparametric one-way ANOVA considering $p < 0.05$ as significative (a: interaction $p = 0.8192$, time $p = 0.3516$, type of implant $p = 0.7091$; b: interaction $p = 0.9728$, time $p = 0.0479$, type of implant $p = 0.7950$; c: interaction $p = 0.1614$, time $p = 0.5894$, type of implant $p = 0.9002$). b.i. = before implant; p.i. = post-implant.

disintegration starting time, which depends on PLGA thickness, the battery remains completely rigid and monolithic (as can be seen in figure 9c,d), therefore the movement of animals should not affect the implanted battery performance nor its functionality.

In order to assess the functionality of the battery as closely as possible to the real conditions, bare and PLGA-coated batteries were implanted in artificial skin as shown in **Figure 10**a. After being completely enclosed in the skin, galvanostatic tests were performed at 1C every 5 days to estimate the evolution of the discharge capacity over 45 days (Figure 10b). Considering that a battery is still operating when more than 80% of its initial capacity is retained, it is apparent that the thicker the PLGA, the longer the operating day. Indeed, the battery can deliver sufficient energy for ≈15, 30, and >45 days for PLGA thicknesses of 40, 110, and 250 µm, respectively. Thus, the PLGA-coating process allows controlling both the operating day and the bio-elimination time of the battery confirming the preliminary tests obtained in Figure 9.

2.4. Wireless Recharging Tests

As proof of feasibility, to be fully implantable, one should be able to recharge the bioresorbable battery without using wires passing

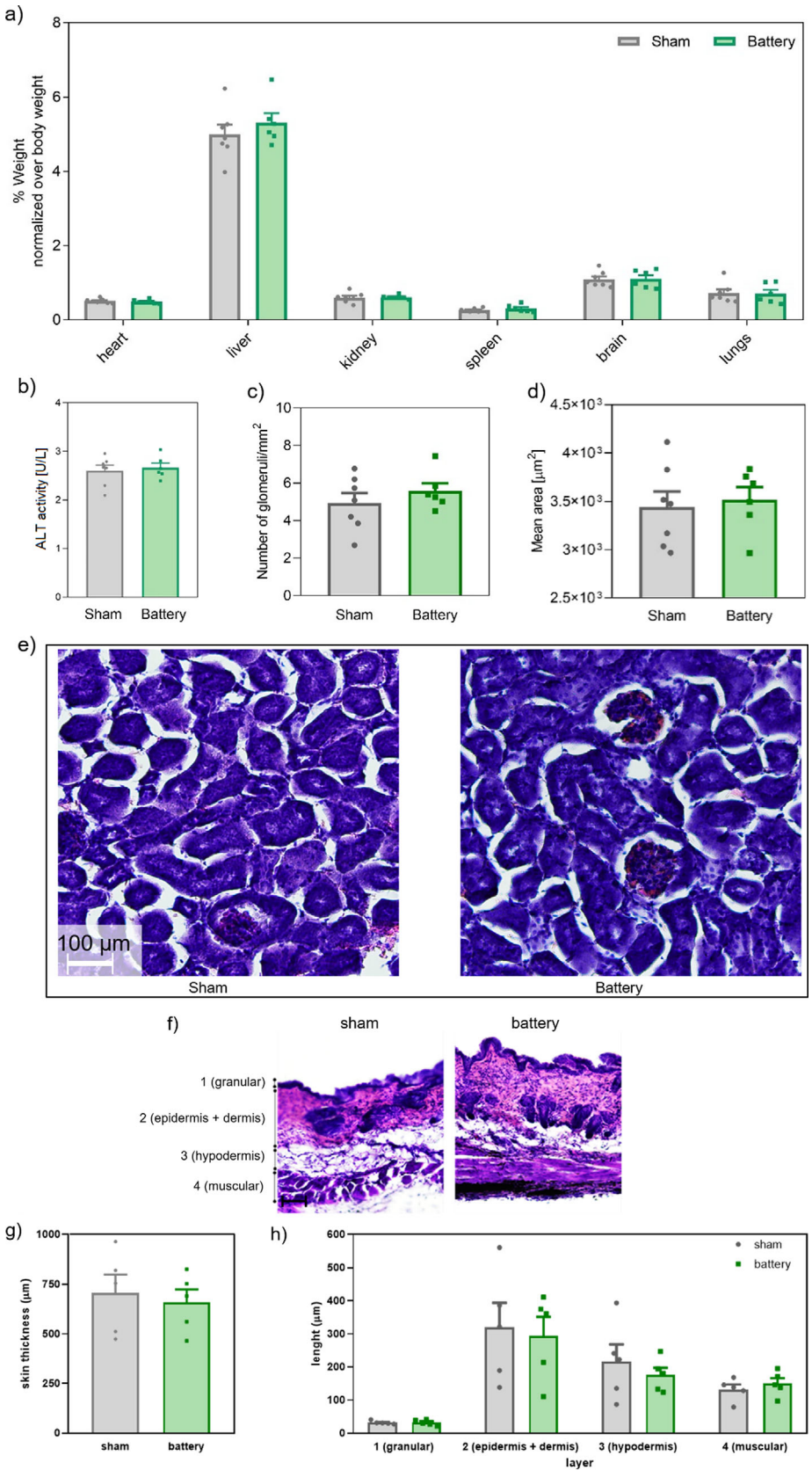

through the skin. Here, a wireless inductive charger was developed in order to recharge the battery from outside the body. The circuit used is presented in **Figure 11a** and is composed of an inductance, a planar coil, which is magnetically coupled to an external transponder. A tuning capacitor is connected in parallel with the inductance in order to optimize the coupling, i.e., the maximum transferred power, between the planar coil and an external transponder. Then a rectifying diode is placed, to keep only positive waves of the alternative current power generated through the coil. After the diode, a smoothing capacitor is used to convert the alternative positive current into a direct current power. Finally, a serial resistor may be added to the circuit to limit the maximum current flowing into the battery.

In this experiment, the external transponder used is a DEMO-CR95HF-A RF transceiver board from ST Microelectronics, made for Near Field Communication (NFC) demonstration. NFC was chosen since it is available in most of the current handheld devices and is already used in Wireless Charging (WLC) of wearable devices such as earbuds, styluses, fitness trackers, or hearing aids.[49–51] WLC operates at a frequency of 13.56 MHz and a 180 pF tuning capacitor was added in parallel with the planar coil of 615 nH to tune this resonant circuit at the same frequency. A smoothing capacitor of 220 nF was added to provide a nearly constant direct current power. In this application, no serial resistor was used (equivalent to $R = 0\ \Omega$) in order to get the maximum current supplied by the charger. To mimic the wireless charging of the implanted battery, the skin of a mouse was laid in between the transponder and the wireless charger as illustrated in Figure 11b.

The variation of potential versus the charge and discharge time shown in Figure 11c were obtained by wirelessly charging the battery for 10 cycles. The corresponding electrochemical performance is presented in Figure 11d. Here, the charging occurred with an average current of 7 mA (≈2C rate) and a discharge current of −7.5 mA. During these cycles, an average of 1 mAh cm^{-2} was found for the specific capacity of the first cycles, which is in line with the results obtained by a conventional wire recharge shown in Figure 4. In this experiment the distance between the transceiver and the wireless charger was 4 mm. Since the magnetic field decreases as the distance between the transceiver and the wireless charger increases, one may also decrease the charging current by moving them further apart. In the experiment described in Figure 11e, we set the distance to 12 mm in order to reach an average current of 3.4 mA during charging. Three cycles of charge and discharge are presented with a maximum of 1.6 mAh cm^{-2} for the specific capacity which is close to 1C rate. By increasing further distance, in the air, between the transceiver and wireless charger, one may expect to reach 1.52 mA with 20 mm and 0.63 mA with a 30 mm distance.

These results highlight the suitability of rechargeable batteries for medical implantable applications. The proposed solution, based on the Near Field Communication (NFC) standard, can also easily be deployed in hospitals or even for self-medical monitoring at home. This study demonstrates a proof of concept of the wireless charging of the bioresorbable battery through a part of the mouse skin. It also shows that power can be transmitted to the wireless charger over a few cm, which could prove useful for a deeply implanted biomedical device. An important point to consider is that part of the transmitted power through inductive coupling can cause local heating at the implanted antenna. During the last experiment, carried at a room temperature of 20.7 °C, a maximum temperature of 27.6 °C was measured at the receiving coil, using a thermal camera FLIR ETS 320, which represents a 6.9 °C rise in temperature. Literature suggests that Poly(lactide), Poly(glycolide), and their related copolymers degradation increases[52] with temperature. In this case, charging through inductive coupling will decrease the implanted device's lifetime if no additional thickness of PLGA is used. These latter results are applicable in air and need to be investigated under in vivo conditions. Regarding the local overheating effect on tissues, perception of pain in adult humans occurs when the basal layer of the epidermis reaches 43 °C,[53] and burn injuries appear when the temperature exceeds 44 °C. In light of this information, an increase of 6.9 °C in our implanted device may potentially start to induce pain. To avoid this scenario, one may consider charging the battery at a lower C-rate, with lower emitted power, in order to reduce local heating during charging.

Even though the described wireless charging circuit is not currently bioresorbable, it has been designed with the potential for future bio-elimination in mind.[1] As a matter of fact, the proposed circuit only embeds 4 components to be operational. For instance, the planar coil and resistor can be patterned in Mg tracks to ensure bio-degradability and literature provides functional examples of biodegradable capacitors and diodes. In the event that more power is needed, one may envision improving this circuit by replacing the rectifying diode with a full diode bridge rectifier.

Table 3 summarizes the main technical features, the key performance indicators, and the wireless recharging characteristics of one prototype. As proof of practical use, a functioning battery has been assembled by stacking three single cells to power continuously two red LEDs (**Figure 12**).

3. Conclusion

To conclude, an alternative fabrication process has been implemented to fabricate a bio-eliminable Na-ion battery show-

Figure 7. a) Organs weight at sacrifice. Data represented as mean ± SE and analysed with non-parametric one-way ANOVA considering $p < 0.05$ as significative (heart: $p = 0.5216$; liver: $p = 0.2949$; kidney: $p = 0.8071$; spleen: $p = 0.4242$; brain: $p > 0.9999$; lungs: $p = 0.7617$). b) ALT activity (U/L). Data represented as mean ± SE and analyzed with a nonparametric t-test considering $p < 0.05$ as the threshold for significance ($p > 0.9999$). c) Number of glomeruli/mm^2 of experimental groups. Data represented as mean ± SE and analyzed with non-parametric one-way ANOVA considering $p < 0.05$ as significative ($p = 0.5338$). d) Mean area (μm^2) of analyzed glomeruli of experimental groups. Data represented as mean ± SE and analyzed with non-parametric one-way ANOVA considering $p < 0.05$ as significative ($p = 0.8357$). e) Representative images of haematoxylin and eosin-stained kidney of sham and battery mice. f) Representative images of haematoxylin and eosin-stained skin of sham and battery mice divided by layers (scale bar = 100 µm). g) Skin thickness (µm) of sham and battery mice. Data represented as mean ± SE and analyzed with non-parametric one-way ANOVA considering $p < 0.05$ as significative ($p = 0.6905$). h) Length (µm) of single skin layers. Data represented as mean ± SE and analyzed with two-way repeated measures ANOVA considering $p < 0.05$ as significative (a: interaction $p = 0.8962$, time $p = 0.007$, type of implant $p = 0.6571$).

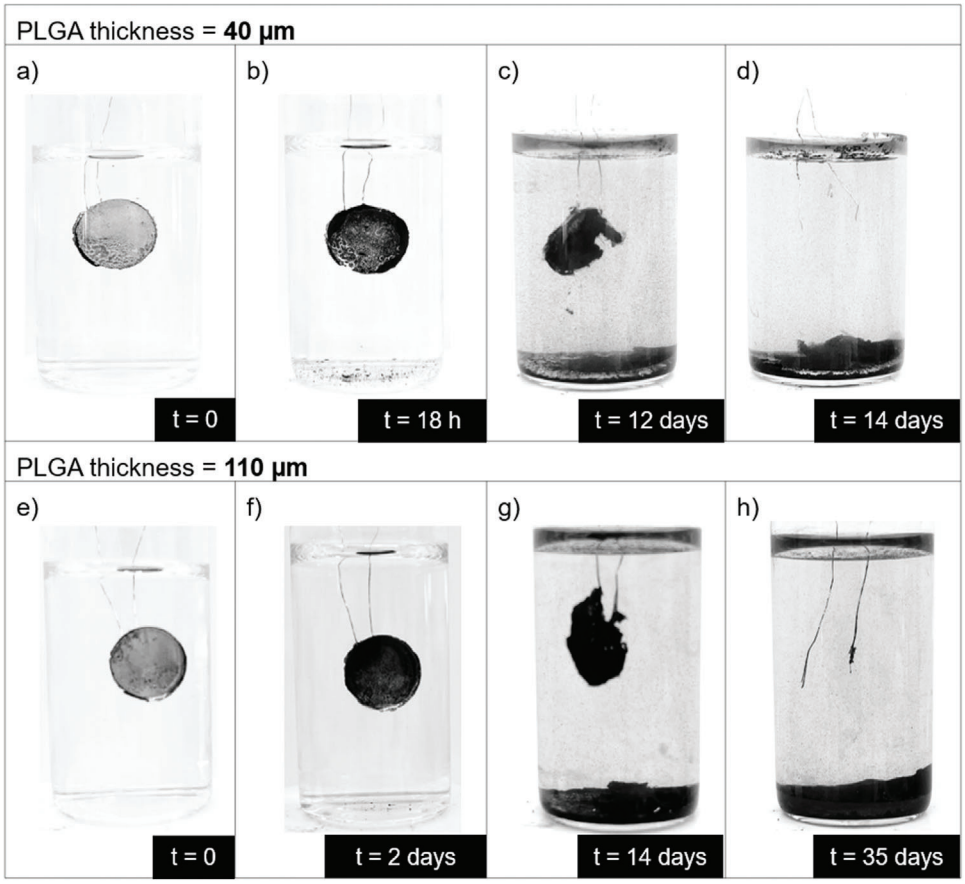

Figure 8. Disintegration evolution of PLGA layer-encapsulated batteries in a PBS static solution. PLGA thickness of a–d) 40 µm and e, f) 110 µm.

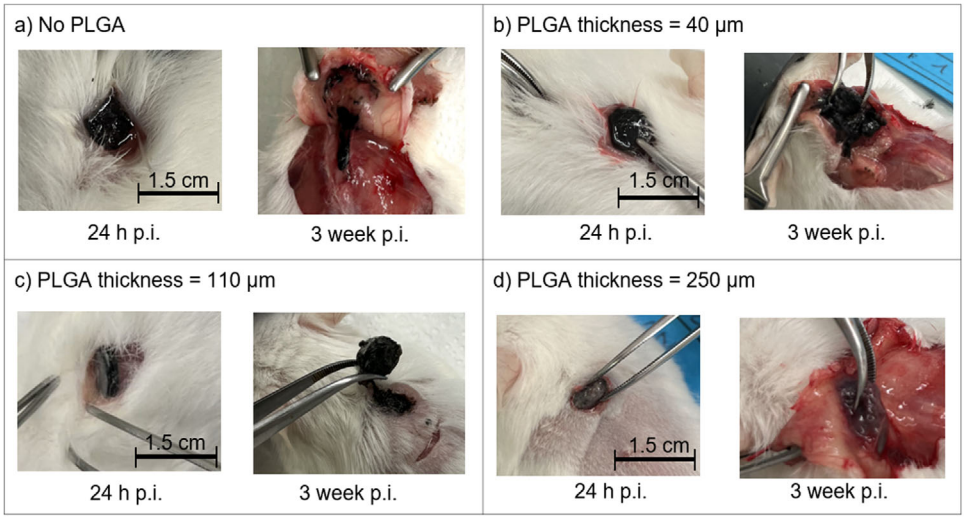

Figure 9. Representative images of a) mice implanted battery without PLGA encapsulation, and b-d) different PLGA coating thicknesses of 40, 110, and 250 µm, respectively. The bio-elimination/bioresorbability is delayed with the increasing thickness of the PLGA coating. (Scale bar = 1,5 cm; p.i. = post-implant).

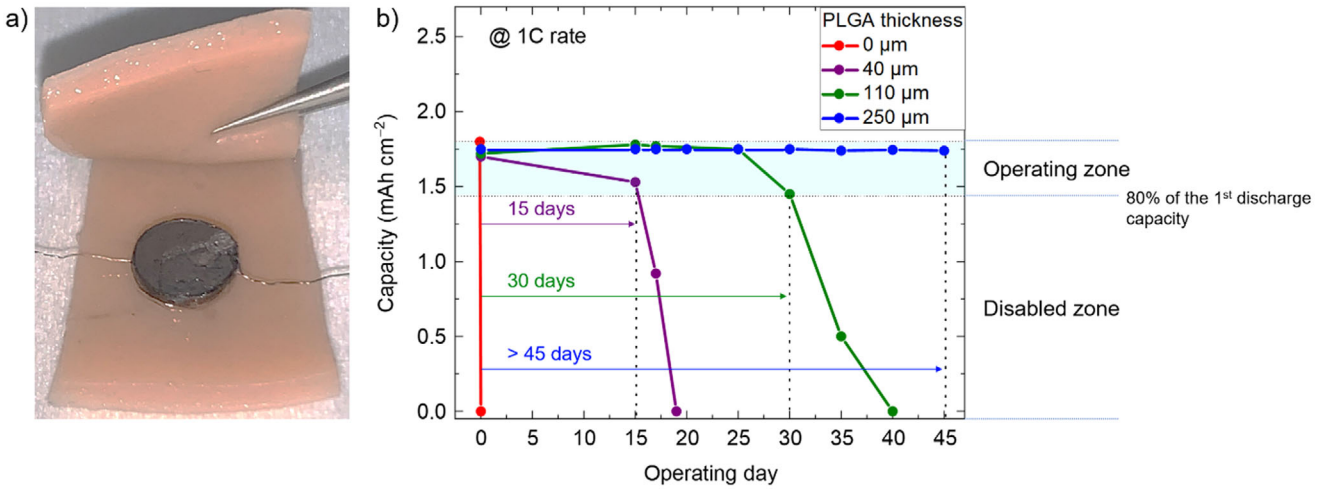

Figure 10. a) Photograph of a PLGA-coated battery (110 µm thick) after implantation in artificial skin for mimicking in vivo conditions. b) Evolution of the discharge capacity as a function of the operating day for bare and PLGA-coated batteries implanted in artificial skin.

ing high electrochemical performance (discharge capacity of 5.1 mAh cm^{-2}) and no sign of toxicity after being disintegrated under in vivo conditions. Solely composed of biocompatible materials that can be safely removed from the body, this subcutaneous implantable and rechargeable all-solid-state battery is able to disintegrate within one day. Actually, all the battery components are rapidly eliminated except for a small amount of carbon black that colors the skin. However, the toxicity tests and the lack of organ damage performed by ex vivo analyses after 3 months confirmed the safety of the approach, and finally, carbon black was almost completely eliminated after 1 year. We demonstrated that operating days and the lifetime of this novel energy storage system after being implanted can be finely controlled by tuning the thickness of the encapsulation layer, paving the way to the design of "on-demand" bio-eliminable batteries that may operate for days or several weeks. In addition, wireless recharge of the battery has been demonstrated through explanted skin using an inductive non-bioresorbable charger circuit to establish the proof-of-concept. Preliminary tests revealed that wireless recharge of the subcutaneously implanted battery has been achieved in 30 min and that recharge would also become possible in 1 h when the battery is deeper implanted. The high versatility of the concept is definitely appealing to address the market of bio-eliminable energy supply for TMDs.

4. Experimental Section

Materials: 3 wt.% carbon-coated sodium titanium phosphate powder, $NaTi_2(PO_4)_3$ (NTP-C) for the anode and sodium manganese oxide powder, $Na_{0.44}MnO_2$ (NMO) for the cathode were purchased from NEI corporation. Sodium alginate, phosphate buffer saline (PBS) tablets, poly(lactic-co-glycolic acid) (lactide: glycolide 65:35), also known as Lactel B6001-1 PLGA with Mw 40000–75000, and sodium sulfate were obtained from Sigma Aldrich. Carbon black (99+% metals basis), a conductive agent, was procured from Thermo Scientific Chemicals. MP5MD – motorized precision press was employed to fabricate electrode pellets. Magnesium granule (99.99 wt.%, Neyco) functioned as an evaporation target for physical vapor deposition. Artificial human tissues (2 N skin toughness) were acquired from SynDaver (USA). The inductive charger is made from single-sided FR4 material. The dielectric material is 0.8 mm, and copper is 35 µm thick. Surface-mounted components were used and manually soldered using SnAgCu alloy. The circuit of the charger on the FR4 printed circuit board was achieved using the LPKF Protolaser S4 laser engraving machine. 0603 packages were used for both capacitors and resistors. A BAV99 high-speed switching diode in a small SOT23 package was used.

Preparation of Gel Electrolyte: Sodium sulfate and alginic acid sodium (aka sodium alginate), were taken at a 2.5:1 weight ratio and dissolved in 10 mL PBS solution under ultrasonication at 80 °C. A gel electrolyte was obtained after 1 h of the sonication. Here, the sodium alginate-based gel electrolyte was intentionally not crosslinked as the use of crosslinking agents such as divalent Ca^{2+} has adversely impacted the bioresorbability feature by increasing the polymer density making it not soluble in aqueous media.[54,55] However, the ionic conductivity of the electrolyte could be ensured by controlling the drying conditions enabling it to retain a bit of moisture.

Pellet Electrode fabrication: An electrode mixture was prepared using active electrode material (NTP-C or NMO) and carbon black in a weight ratio of 86:10. Additionally, water-based gel electrolyte (290 µL) was added in an amount equivalent to 4 wt.% of its dry state. This wet electrode mix was filled in the round mold die set to make a pellet form by hydraulic press machine with an applied pressure of 2 tons cm^{-2} that ensured the cohesion of the active material grains with the carbon black and the SA binder for achieving a reliable bonding of electrodes. The pellet electrodes of 0.74 cm diameter were obtained and subjected to dry for 2 h in a 90 °C vacuum oven.

Full Cell Assembly: first, the gel electrolyte was drop-casted onto a smooth surface and the electrode pellet was pressed against it while drying in the oven for 15 min at 90 °C until the visual observation where the gel layer dried thoroughly. After drying, another pellet electrode with a thin layer of gel was prepared similarly. Then, the electrolyte surface of each surface was slightly wet before being sandwiched face to face, and a physical force was applied to remove the air gap possibly trapped during the sandwich. Then, this cell assembly was dried at 90 °C for 15 min.

Electrical Connections: All electrical connections were ensured by Mg interconnects and Mg wire bonding without the use of any soldering paste. The connecting wires were impressed on the backside of the pellet electrodes prior to the Mg evaporation process to minimize the contact resistance. Furthermore, to avoid leakage of the PBS solution through the interconnection, PLGA encapsulation was extended along the testing wires outwardly while dipping the battery into the PLGA solution.

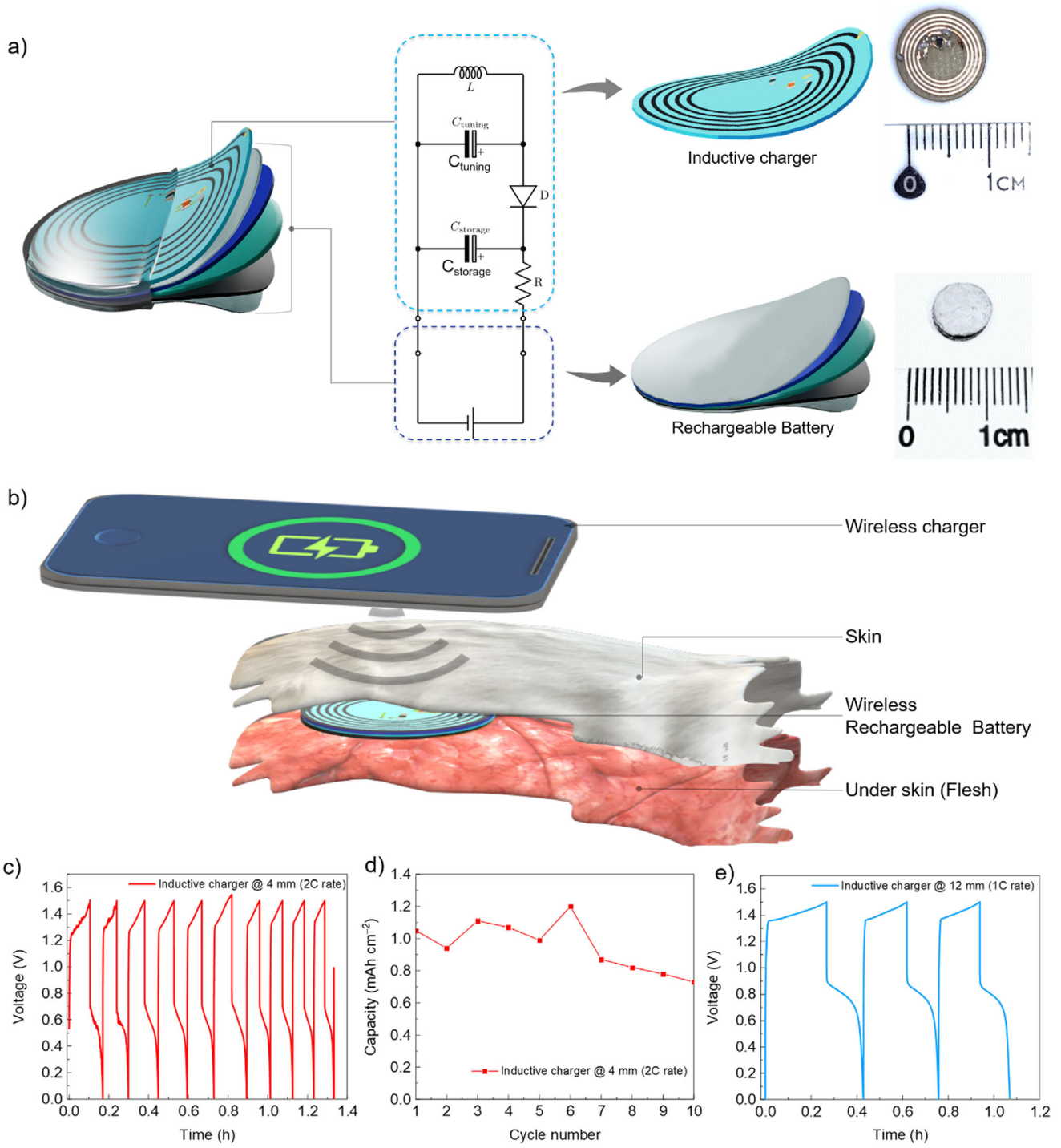

Figure 11. a) Rechargeability test for the final circuit presenting the interconnection of the bioresorbable battery. b) Model RF transmitter charger. c) Variation of voltage versus time of charge and discharge for 10 cycles using the inductive charger at a distance of 4 mm and d) corresponding electrochemical performance. e) Variation of voltage versus time of charge and discharge for 3 cycles using the inductive charger at a distance of 12 mm.

Mg Deposition: The assembled full cell was subjected to Mg evaporation using a metal evaporator operating on the principle of Joules effect under a high vacuum condition of 5×10^{-6} mbar. To prevent short circuits caused by Mg deposition at the electrolyte interface, the curved surface of the full cell was firmly shielded with Teflon tape. A thin film of Mg, 600 nm in thickness, was subsequently deposited as a current collector on both sides of the assembled cell.

PLGA Encapsulation: A dip-casting PLGA solution was prepared by dissolving 200 mg of PLGA pellets in 1 mL of acetone solvent. The fully assembled battery was dipped into this viscous solution and then

Table 3. Technical characteristics and key performance indicators corresponding to the all-solid-state bio-eliminable battery.

Main Features	
Diameter	0.74 cm
Thickness	0.12 cm
Surface	0.43 cm^2
Volume	0.05 cm^3
Mass	90 mg
Bio-elimination time	One day–several months
Key Performance Indicators @ C/2 rate	
1st discharge capacity	1.2 mAh
Capacity retention	83% after 50 cycles
Energy	0.78 mWh
Power	1.17 mW
Wireless recharging characteristics	
Recharge at 4 mm	30 min
Recharge at 12 mm	1 h

transferred to an oven at 100 °C to facilitate the rapid evaporation of the volatile acetone, forming a conformal PLGA layer. Each iteration of this process resulted in the formation of a ≈40 µm PLGA film, as measured for the given PLGA/acetone content.

Physical and Electrochemical Characterization: CARL ZEIS-S/Ultra 55 Scanning Electron Microscope (SEM) machine was utilized for topographic analysis associated with the EDX for the elemental mapping of a cross-section of all solid-state bioresorbable batteries. The sealing of the full cell with PLGA gel was performed inside the glovebox Jacomex, Model GP (concept) which allowed to deoxygenate the full cell before the encapsulation. The galvanostatic charge and discharge measurements were carried out by means of VMP3 (Bio Logic) potentiostat–galvanostat at a constant temperature (298 K). Alliance Concept EVA450 metal evaporator was employed for magnesium evaporation. In vitro tests at constant temperature (37 °C) were performed with CTS Clima temperature system. For inductive charger characterization, wireless galvanostatic cycling was achieved by designing specific equipment using a Keithley 2602B source measure unit (SMU) and a CR95HF RF transceiver demonstration board from ST Microelectronics. It operates as follows: channel A of the SMU records the voltage across the battery, and channel B records the current flowing into the battery. During charging, the field emitted by the transceiver is on, and the inductive charger produces a close-to-constant current that goes to the battery until a maximum voltage target is reached. Then, the electromagnetic field of the transceiver is turned off, and a constant negative current is applied from channel A to discharge the battery. When 0 V is reached across the battery, the charging phase starts again, and charge-discharge cycles occur. During these cycles, voltage and current are recorded, and specific capacity is calculated from the discharging phase.

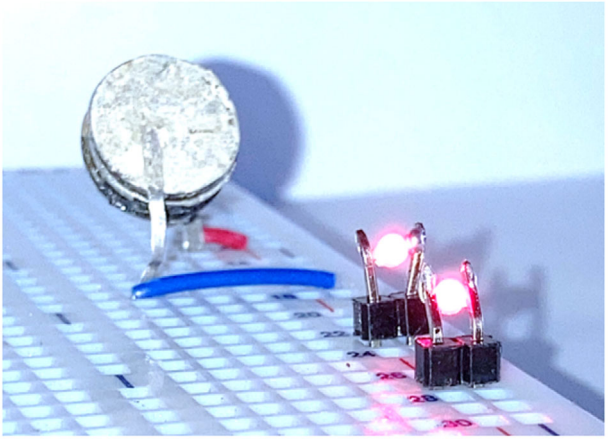

Figure 12. Visual demonstration of lighting red LEDs powered by the bioresorbable battery, showcasing its potential for use in temporary microelectronic systems.

In Vitro Study of Electrochemical Functionality of Battery Under Artificial Skin (A Simulated Physiological Condition): Na-ion batteries with PLGA encapsulation layers of various thicknesses were designed for in vitro testing to evaluate their electrochemical performance and degradation behavior under simulated physiological conditions using the artificial skin. As obtained synthetic skin sample (SynDaver, ≈3.5 × 2.5 cm, 1.5 mm thick) was pre-soaked in phosphate-buffered saline (PBS) solution to mimic the natural hydration. Batteries were sandwiched between two layers of wet artificial skin. For comparison, a battery without encapsulation was also placed within the same setup. Periodically, galvanostatic charge-discharge measurements were recorded at 1C rate for each battery. Fresh PBS solution was passed through the setup every two days to maintain the natural hydration level and consistent wettability of the skin surrounding the batteries. The primary goal was to monitor the capacity retention to evaluate the onset and progression of battery degradation.

Animals for In Vivo and Ex Vivo Experiments: For this study, CD1 and C57 mice strains (with the same behavioral and histological predictivity) were used.[56,57] Three-month-old (at the start of the experiment) CD1 ($n = 14$) and C57 ($n = 2$) male and female mice from the colony of the University of Modena and Reggio Emilia facility were used for in vivo and ex-vivo studies. The progenitors for the colony were purchased from Charles River Laboratories Italia s.r.l. (Calco-Milano, Italy). Mice were housed in a pathogen-free facility and kept in conditioned rooms with stable temperature (21 ± 0.5 °C) and humidity (60%), on a 12 h light/dark cycle with food and water available ad libitum. All animal procedures were approved by the Committee on Animal Health and Care of the University of Modena and Reggio Emilia and conducted in accordance with National Institutes of Health guidelines [CEE Council 89 609; Italian DL 26/2014, authorization n° 979/2020/PR]. All efforts were made to minimize animal suffering and to reduce the number of animals used in this study.

Battery Implantation Procedure for In Vivo And Ex Vivo Experiments: Animals were randomly assigned to 2 experimental groups respecting gender proportions: the Sham group (mice that underwent surgery without having any battery implanted, $n = 7$) and the Battery group (mice with implanted battery, $n = 7$). The other two mice were also implanted with the battery and used to follow the biodegradation/bioelimination of it for one year.

Before surgery procedures, mice, under anesthesia with inhaled isoflurane, were shaved in the back and underwent surgery. Upper back skin was disinfected with betadine, lifted, and incised, and a subcutaneous pouch of 1.5 × 1.5 cm was created to insert the battery. The incision was sutured by applying a surgical stitch and treated with Neuflan gel (Neomycin 0.5 g/Flucinolone acetonide 0.025 g/Lidocaine 2.5 g) to minimize local post-operative pain and the risk of infections.

In Vivo Toxicity Evaluation: To exclude battery toxicity and confirm their biocompatibility, every 2 weeks for 3 months several parameters of general integrity were evaluated using a modified SHIRPA protocol.[58] Briefly, monitored weight throughout the experimental period (3 months) and the weight of each animal was normalized to the weight the animal had prior to implant. Macro parameters were also observed and scored such as activity status, tremor, lacrimation, eyelid closure, fur appearance, whisker movement, and defecation, with a score 0–1 where 0 = absent and 1 = present parameters. Additionally, to exclude acute inflammatory reaction due to implantation, body temperature was measured rectally with the aid of vaseline cream and checked at different time points (namely, before implant, 24, 48, 72 h, 7 and 14 days after implant). Furthermore, to assess locomotion and anxiety, which are the first parameters in mice that undergo a change in case of toxicity,[59,60] the open field (OF) test was performed once a month for 3 months. A behavioral test was performed by an operator unaware of the experimental group to avoid bias. Animal behavior

was recorded and automatically analyzed with ANY-maze Video Tracking system (Stoelting). The motor activity and exploration in a new environment were assessed in the OF test. Mice were placed in the center of an open wooden chamber (50 × 50 × 40 cm) with dark walls and allowed to explore freely for 10 min. The open space was virtually subdivided into 3 zones (Figure S4, Supporting Information), namely, periphery (within 10 cm of the walls), center (the rest of the arena), and corners for assessment of anxiety. Traveled distance, maximum speed, and time spent in each zone were automatically recorded. The time spent in the center of the arena was considered as an anxiety index (mice spend more time in the periphery when they are anxious).[59,60] The apparatus was thoroughly wiped with 70% ethanol after each test to avoid olfactory cues.

In Vivo Biodegradation/Bioelimination of the Battery: A pilot study to verify the evolution of the biodegradation/bioelimination of the battery in vivo, at three different time points (namely, 24 h, 3 months, and 1 year after implant) was carried out. For ethical reasons, only 2 animals were used according to the 3 R principle (replace, reduce, refine; Guideline 2010/63/UE, Italian D.L n. 26, 4th March 2014). Implantation was performed as previously reported and if the battery was still present under the back skin of the implanted mice was observed. Sham mice also underwent the same surgical procedures.

Sacrifice, Blood, and Organ Collection for Ex Vivo Toxicity Evaluation: After 3 months from surgery, under general anesthesia with inhaled isoflurane, blood was collected, let coagulate at room temperature for 20 min, and then centrifuged at 1200 g for 15 min to extract serum to evaluate hepatic markers. Additionally, organs (liver, spleen, kidney, heart, lung, brain, and back skin) were collected and weighted to evaluate any macroscopic alteration.

Hepatic Toxicity Evaluation: Serum Alanine Transaminase (ALT) activity (U/L), index of hepatic toxicity, was evaluated with ALT activity assay according to manufacturer instructions (Sigma-Aldrich). Briefly, ALT activity was evaluated through an enzymatic colorimetric assay, using 20 µL of serum per sample, with absorbance reading at 570 nm (Multiskan FC, Thermo Scientific) and calculated with linear regression method, using a pyruvate standard curve.

Histological Analysis of Kidney and Skin: Post-fixed kidney and skin were immersed in 20% sucrose-PBS for 2 days, and then 30% sucrose-PBS for 3 days. The kidney and skin samples were frozen and included in the histomount mounting medium using dry ice and stored at −80 °C until use. Kidney and skin samples were sectioned (Leica CM1520 cryostat) at −27 °C into 20 and 40 µm thick transversal slices respectively and stored on slides at −20 °C until use. The slides were air-dried at room temperature for 4 h prior to hematoxylin and eosin histological staining that was conducted according to validated protocols.[5] Histological images were captured using an optical microscope (Nikon Eclipse Ci) with a 10× objective.

The thickness of different skin layers (granular layer, epidermis and dermis, hypodermis, and muscular cell layer) was measured through length tool measurement of NIS software.

Statistical Analysis: Statistical analysis was performed using one-way analysis of variance (ANOVA) Kruskal-Wallis non-parametric test, Mann–Whitney U test, or two-way repeated-measures ANOVA, with the appropriate posthoc test, such as Dunn or Sidak's multiple comparisons test, using GraphPad Prism. Significance threshold was set at $p < 0.05$, with $p < 0.05$*; <0.01**; <0.001***; <0.0001****.

Supporting Information

Supporting Information is available from the Wiley Online Library or from the author.

Acknowledgements

This work was partially funded by the European Union Horizon Europe program under grant agreement No 101046946 (RESORB) and by the Programme de Recherche PEPR Batteries France 2030 under grant agreement No ANR-23-PEBA-0006 (SIMBA); the authors also thank the technical support from ID-Fab (Prototyping platform: project funded by the European Regional Development Fund, the French state and local authorities). V.K.A.M. and B.L.V. contributed equally to this work.

Conflict of Interest

The authors declare no conflict of interest.

Data Availability Statement

The data that support the findings of this study are available from the corresponding author upon reasonable request.

Keywords

bioresorbable batteries, implantable system, Na-ion technology, predesigned lifetime, temporary medical devices, wireless recharging

Received: November 28, 2024
Revised: January 8, 2025
Published online:

[1] J. Koo, M. R. MacEwan, S.-K. Kang, S. M. Won, M. Stephen, P. Gamble, Z. Xie, Y. Yan, Y.-Y. Chen, J. Shin, N. Birenbaum, S. Chung, S. B. Kim, J. Khalifeh, D. V. Harburg, K. Bean, M. Paskett, J. Kim, Z. S. Zohny, S. M. Lee, R. Zhang, K. Luo, B. Ji, A. Banks, H. M. Lee, Y. Huang, W. Z. Ray, J. A. Rogers, *Nat. Med.* **2018**, *24*, 1830.

[2] S.-K. Kang, R. K. J. Murphy, S.-W. Hwang, S. M. Lee, D. V. Harburg, N. A. Krueger, J. Shin, P. Gamble, H. Cheng, S. Yu, Z. Liu, J. G. McCall, M. Stephen, H. Ying, J. Kim, G. Park, R. C. Webb, C. H. Lee, S. Chung, D. S. Wie, A. D. Gujar, B. Vemulapalli, A. H. Kim, K.-M. Lee, J. Cheng, Y. Huang, S. H. Lee, P. V. Braun, W. Z. Ray, J. A. Rogers, *Nature* **2016**, *530*, 71.

[3] G. Yao, L. Kang, C. Li, S. Chen, Q. Wang, J. Yang, Y. Long, J. Li, K. Zhao, W. Xu, W. Cai, Y. Lin, X. Wang, *Proc. Natl. Acad. Sci. U.S.A.* **2021**, *118*, 2100772118.

[4] Y. S. Choi, R. T. Yin, A. Pfenniger, J. Koo, R. Avila, K. Benjamin Lee, S. W. Chen, G. Lee, G. Li, Y. Qiao, A. Murillo-Berlioz, A. Kiss, S. Han, S. M. Lee, C. Li, Z. Xie, Y.-Y. Chen, A. Burrell, B. Geist, H. Jeong, J. Kim, H.-J. Yoon, A. Banks, S.-K. Kang, Z. J. Zhang, C. R. Haney, A. V. Sahakian, D. Johnson, T. Efimova, Y. Huang, et al., *Nat. Biotechnol.* **2021**, *39*, 1228.

[5] M. Corsi, A. Paghi, S. Mariani, G. Golinelli, A. Debrassi, G. Egri, G. Leo, E. Vandini, A. Vilella, L. Dähne, D. Giuliani, G. Barillaro, *Adv. Sci.* **2022**, *9*, 2202062.

[6] Y. Zhang, G. Lee, S. Li, Z. Hu, K. Zhao, J. A. Rogers, *Chem. Rev.* **2023**, *123*, 11722.

[7] H. Sheng, X. Zhang, J. Liang, M. Shao, E. Xie, C. Yu, W. Lan, *Adv. Healthcare Mater.* **2021**, *10*, 2100199.

[8] S. Mukherjee, A. Albertengo, T. Djenizian, *Energy Storage Mater.* **2021**, *42*, 773.

[9] S. Stauss, I. Honma, *Bull. Chem. Soc. Jpn.* **2018**, *91*, 492.

[10] T. Mei, C. Wang, M. Liao, J. Li, L. Wang, C. Tang, X. Sun, B. Wang, H. Peng, *J. Mater. Chem. A* **2021**, *9*, 10104.

[11] X. Huang, D. Wang, Z. Yuan, W. Xie, Y. Wu, R. Li, Y. Zhao, D. Luo, L. Cen, B. Chen, H. Wu, H. Xu, X. Sheng, M. Zhang, L. Zhao, L. Yin, *Small* **2018**, *14*, 1800994.

[12] X. Huang, H. Hou, B. Yu, J. Bai, Y. Guan, L. Wang, K. Chen, X. Wang, P. Sun, Y. Deng, S. Liu, X. Cai, Y. Wang, J. Peng, X. Sheng, W. Xiong, L. Yin, *ACS Nano* **2023**, *17*, 5727.

[13] V. García-Caballero, S. Lorca, M. Villa-Moreno, Á. Caballero, J. J. Giner-Casares, A. J. Fernández-Romero, M. Cano, *Energy Fuels* **2023**, *37*, 18210.
[14] M. Mohammadifar, S. Choi, *Adv. Mater. Technol.* **2017**, *2*, 1700127.
[15] M. Angell, C.-J. Pan, Y. Rong, C. Yuan, M.-C. Lin, B.-J. Hwang, H. Dai, *Proc. Natl. Acad. Sci. U.S.A.* **2017**, *114*, 834.
[16] Y. Dong, J. Li, F. Yang, Y. Wang, Z. Zhang, J. Wang, Y. Long, X. Wang, *ACS Appl. Mater. Interfaces* **2021**, *13*, 14275.
[17] G. Zhang, F. Geng, T. Zhao, F. Zhou, N. Zhang, S. Zhang, C. Deng, *ACS Appl. Mater. Interfaces* **2018**, *10*, 42268.
[18] Z. Guo, Y. Zhao, Y. Ding, X. Dong, L. Chen, J. Cao, C. Wang, Y. Xia, H. Peng, Y. Wang, *Chem* **2017**, *3*, 348.
[19] Y. J. Kim, A. Khetan, W. Wu, S. Chun, V. Viswanathan, J. F. Whitacre, C. J. Bettinger, *Adv. Mater.* **2016**, *28*, 3173.
[20] Z. Li, D. Young, K. Xiang, W. C. Carter, Y. Chiang, *Adv. Energy Mater.* **2013**, *3*, 290.
[21] X. Zhou, A. Zhao, Z. Chen, Y. Cao, *Electrochem. Commun.* **2021**, *122*, 106897.
[22] M. Soleimanzade, M. Radaelli, J. Manidi, M. Bahdanchyk, A. Vicenzo, *Batteries* **2023**, *9*, 428.
[23] X. Cao, Y. Yang, *Mater. Lett.* **2018**, *231*, 183.
[24] A. Dodero, S. Alberti, G. Gaggero, M. Ferretti, R. Botter, S. Vicini, M. Castellano, *Adv. Mater. Interfaces* **2021**, *8*, 2100809.
[25] L. Marchi, F. Dinelli, P. Maccagnani, V. Costa, T. Chenet, G. Belletti, M. Natali, M. Cocchi, M. Bertoldo, M. Seri, *ACS Sustainable Chem. Eng.* **2022**, *10*, 15608.
[26] A. Wang, Y. Tu, S. Wang, H. Zhang, F. Yu, Y. Chen, D. Li, *Polymers* **2022**, *14*, 4552.
[27] H. Yang, Y. Liu, L. Kong, L. Kang, F. Ran, *J. Power Sources* **2019**, *426*, 47.
[28] S. Ramesh, R. Shanti, E. Morris, *Carbohydr. Polym.* **2012**, *87*, 701.
[29] R. Luo, H. Jiang, B. Du, S. Zhou, Y. Zhu, *AIP Adv.* **2019**, *9*, 035341.
[30] G. Deysher, Y.-T. Chen, B. Sayahpour, S. W.-H. Lin, S.-Y. Ham, P. Ridley, A. Cronk, E. A. Wu, D. H. S. Tan, J.-M. Doux, J. A. S. Oh, J. Jang, L. H. B. Nguyen, Y. S. Meng, *ACS Appl. Mater. Interfaces* **2022**, *14*, 47706.
[31] E. Ventosa, *Curr. Opin. Chem. Eng.* **2022**, *37*, 100834.
[32] X. Yu, A. Manthiram, *Sustain. Energy Fuels* **2018**, *2*, 1452.
[33] L. Yin, H. Cheng, S. Mao, R. Haasch, Y. Liu, X. Xie, S. Hwang, H. Jain, S. Kang, Y. Su, R. Li, Y. Huang, J. A. Rogers, *Adv. Funct. Mater.* **2014**, *24*, 645.
[34] G. Ma, Y. Zhao, K. Huang, Z. Ju, C. Liu, Y. Hou, Z. Xing, *Electrochim. Acta* **2016**, *222*, 36.
[35] E. Oz, S. Altin, S. Avci, *J. Solid State Chem.* **2023**, *318*, 123741.
[36] I. Huang, Y. Zhang, H. M. Arafa, S. Li, A. Vazquez-Guardado, W. Ouyang, F. Liu, S. Madhvapathy, J. W. Song, A. Tzavelis, J. Trueb, Y. Choi, W. J. Jeang, V. Forsberg, E. Higbee-Dempsey, N. Ghoreishi-Haack, I. Stepien, K. Bailey, S. Han, Z. J. Zhang, C. Good, Y. Huang, A. J. Bandodkar, J. A. Rogers, *Energy Environ. Sci.* **2022**, *15*, 4095.
[37] M. Tsang, A. Armutlulu, A. W. Martinez, S. A. B. Allen, M. G. Allen, *Microsyst. Nanoeng.* **2015**, *1*, 15024.
[38] X. Jia, C. Wang, V. Ranganathan, B. Napier, C. Yu, Y. Chao, M. Forsyth, F. G. Omenetto, D. R. MacFarlane, G. G. Wallace, *ACS Energy Lett.* **2017**, *2*, 831.
[39] Y. J. Kim, S.-E. Chun, J. Whitacre, C. J. Bettinger, *J. Mater. Chem. B* **2013**, *1*, 3781.
[40] L. Yin, X. Huang, H. Xu, Y. Zhang, J. Lam, J. Cheng, J. A. Rogers, *Adv. Mater.* **2014**, *26*, 3879.
[41] X. Jia, C. Wang, C. Zhao, Y. Ge, G. G. Wallace, *Adv. Funct. Mater.* **2016**, *26*, 1454.
[42] Y. J. Kim, W. Wu, S.-E. Chun, J. F. Whitacre, C. J. Bettinger, *Proc. Natl. Acad. Sci. U.S.A.* **2013**, *110*, 20912.
[43] J. de Bruin Jordaan, M. Postema, C. S. Carlson, K. J. Nixon, *Curr. Dir. Biomed. Eng.* **2023**, *9*, 9.
[44] R. Lalonde, M. Filali, C. Strazielle, *Curr. Protoc.* **2021**, *1*, e135.
[45] N. M. Davis, M. M. Lissner, C. L. Richards, V. Chevée, A. S. Gupta, F. C. Gherardini, D. S. Schneider, *mBio* **2021**, *12*, 10.
[46] C. F. Adhipandito, S.-H. Cheung, Y.-H. Lin, S.-H. Wu, *Int. J. Mol. Sci.* **2021**, *22*, 11182.
[47] J. G. Croissant, Y. Fatieiev, N. M. Khashab, *Adv. Mater.* **2017**, *29*, 1604634.
[48] X. Li, B. Wang, S. Zhou, W. Chen, H. Chen, S. Liang, L. Zheng, H. Yu, R. Chu, M. Wang, Z. Chai, W. Feng, *J. Nanobiotechnol.* **2020**, *18*, 45.
[49] D. S. Bhatti, S. Saleem, A. Imran, Z. Iqbal, A. Alzahrani, H. Kim, K.-I. Kim, *Sensors* **2022**, *22*, 7722.
[50] M. Bouklachi, M. Biancheri-Astier, A. Diet, Y. Le Bihan, *IEEE J. Radio Frequency Ident.* **2020**, *4*, 107.
[51] K. Katiyar, H. Gupta, A. Gupta, in 2014 5th Int. Conf.– Confluence The Next Generation Information Technology Summit (Confluence), IEEE **2014**, 365–372.
[52] L. Geddes, L. Carson, E. Themistou, F. Buchanan, *Polym. Test.* **2020**, *91*, 106853.
[53] N. A. Martin, S. Falder, *Burns* **2017**, *43*, 1624.
[54] O. Saswat, P. H. Maheshwari, *Emergent. Mater.* **2023**, *6*, 197.
[55] H. Malektaj, A. D. Drozdov, J. deClaville Christiansen, *Polymers* **2023**, *15*, 3012.
[56] A. W. Hayes, P. Pressman, J. F. Hardisty, S. B. Harris, K. Weber, *Regulat. Toxicol. Pharmacol.* **2020**, *111*, 104557.
[57] L. Cui, L. Shi, D. Li, X. Li, X. Su, L. Chen, Q. Jiang, M. Jiang, J. Luo, A. Ji, *Front. Pharmacol.* **2020**, *11*, 199.
[58] D. C. Rogers, E. M. C. Fisher, S. D. M. Brown, J. Peters, A. J. Hunter, J. E. Martin, *Mammalian. Genome.* **1997**, *8*, 711.
[59] E. Daini, E. Vandini, M. Bodria, W. Liao, C. Baraldi, V. Secco, A. Ottani, M. Zoli, D. Giuliani, A. Vilella, *Front. Immunol.* **2023**, *13*.
[60] A.-K. Kraeuter, P. C. Guest, Z. Sarnyai, *Pre-Clin. Models* **2019**, 99.